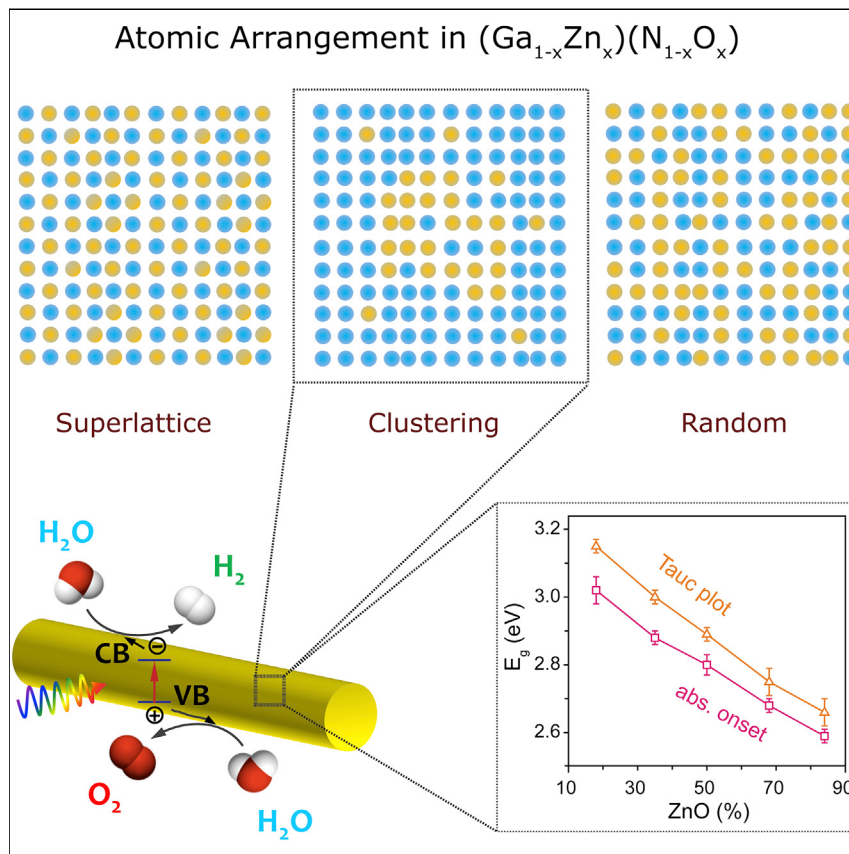


Article

Atomic arrangement matters: band-gap variation in composition-tunable $(\text{Ga}_{1-x}\text{Zn}_x)(\text{N}_{1-x}\text{O}_x)$ nanowires



$(\text{Ga}_{1-x}\text{Zn}_x)(\text{N}_{1-x}\text{O}_x)$ nanowires with fully tunable compositions are synthesized via a customized chemical vapor deposition strategy. Atomic-scale element distribution is found to play a dominant role in determining the electronic band structure of $(\text{Ga}_{1-x}\text{Zn}_x)(\text{N}_{1-x}\text{O}_x)$ and causes a continuous band-gap reduction with increasing ZnO content. This finding highlights the vital role of atomic arrangement engineering in modulating the energy band structures of nonisovalent semiconductor alloys at the atomic scale.

Kai Zhang, Tao Chen, Yasir Abbas, ..., Jing Zhang, Yimin Xuan, Jian Ru Gong

jzhang@ihep.ac.cn (J.Z.)
ymxuan@nuaa.edu.cn (Y.X.)
gongjr@nanoctr.cn (J.R.G.)

HIGHLIGHTS

$(\text{Ga}_{1-x}\text{Zn}_x)(\text{N}_{1-x}\text{O}_x)$ nanowires with tunable compositions are successfully synthesized

A strong clustering tendency exists in the synthesized $(\text{Ga}_{1-x}\text{Zn}_x)(\text{N}_{1-x}\text{O}_x)$ nanowires

Band alignments between the clusters and the host material dominate the band structures

Atomic arrangement engineering provides an additional tool for band-gap regulation



Benchmark

First qualification/assessment of material properties and/or performance

Zhang et al., Matter 4, 1054–1071
March 3, 2021 © 2020 Elsevier Inc.
<https://doi.org/10.1016/j.matt.2020.12.024>



Article

Atomic arrangement matters: band-gap variation in composition-tunable $(\text{Ga}_{1-x}\text{Zn}_x)(\text{N}_{1-x}\text{O}_x)$ nanowires

Kai Zhang,^{1,2,6} Tao Chen,^{3,6} Yasir Abbas,^{1,6} Saad Ullah Jan,^{1,4} Zhaohui Zhou,⁵ Shengqi Chu,³ Guancai Xie,^{1,4} Sana Ullah,^{1,4} Muhammad Zain Akram,^{1,4} Jing Zhang,^{3,*} Yimin Xuan,^{2,*} and Jian Ru Gong^{1,4,7,*}

SUMMARY

We synthesized single-crystal $(\text{Ga}_{1-x}\text{Zn}_x)(\text{N}_{1-x}\text{O}_x)$ nanowires with fully tunable compositions ($0 < x < 1$) using a customized chemical vapor deposition strategy. Despite the uniform distributions of component elements at the nanometer scale, X-ray absorption fine structure analysis in combination with *ab initio* multiple-scattering calculation verified the existence of a strong clustering tendency, i.e., the energetic preference of the valence-matched Ga-N and Zn-O pairs, in the synthesized nanowires. The strong clustering tendency plays a dominant role in determining the electronic band structures of the nanowires, causing a continuous band-gap reduction with increasing ZnO content, which is interpreted via a type II band alignment among the intracrystalline heterojunctions formed between the incorporated clusters and the host material. This, ultimately, makes the sample with the highest ZnO content show the highest water-splitting activity. Atomic arrangement engineering will provide an additional tool for band-gap engineering of semiconductor alloys, greatly benefiting the development of new functional materials for energy conversion applications.

INTRODUCTION

Sunlight-driven overall water splitting using semiconductor photocatalysts represents a promising strategy to convert solar energy into chemical energy and store it in a sustainable, clean, and storable hydrogen fuel.^{1–4} However, natural semiconductors available for overall water splitting are still very limited, because of the stringent requirements of water splitting on the energy band structures of semiconductor photocatalysts.^{5–7} Alloying of semiconductors with the same crystal structures but different optoelectronic properties, which is a facile and effective strategy to achieve new and especially tunable band gaps, has gained certain achievements in triggering the splitting of pure water into hydrogen and oxygen gases in recent years.^{8,9} Nonetheless, most of the efforts are devoted to controlling the size, shape, and composition of these semiconductor alloys,^{3,4,10–12} while little attention is paid to the atomic-scale element distribution, which is a characteristic structural “degree of freedom,” being decisive in controlling the mechanical, optical, electronic, and/or catalytic properties of multiple element alloys.^{13,14}

$(\text{Ga}_{1-x}\text{Zn}_x)(\text{N}_{1-x}\text{O}_x)$, a typical nonisovalent solid-solution semiconductor composed of GaN and ZnO, offers a perfect combination of properties desired for water splitting, i.e., appropriate band edges, visible-light response, and resistance to photocorrosion.^{15–19} Thus, it has been reported to be one of the most promising

Progress and potential

Alloying of semiconductors has gained a certain improvement in regulating their band structures for overall water splitting. However, little attention has been paid to the arrangement of the constituent elements at the atomic scale. Particularly, the variation in the band gap of a nonisovalent alloy photocatalyst, $(\text{Ga}_{1-x}\text{Zn}_x)(\text{N}_{1-x}\text{O}_x)$, following the change in composition, as well as the underlying mechanisms, has been under intense debate, because of the ambiguous atomic-scale element distribution. Here, using composition-tunable single-crystal $(\text{Ga}_{1-x}\text{Zn}_x)(\text{N}_{1-x}\text{O}_x)$ nanowires grown via chemical vapor deposition as a model system, we verify the energetic preference of the valence-matched Ga-N and Zn-O pairs in $(\text{Ga}_{1-x}\text{Zn}_x)(\text{N}_{1-x}\text{O}_x)$ alloys and demonstrate the dominant role of this clustering tendency in controlling their electronic band structures. These findings highlight the vital role of atomic arrangement engineering in modulating the band structures of semiconductor alloys.



photocatalysts for visible-light-driven overall water splitting, with a reported apparent quantum efficiency of 5.9% ($x = 0.18$) under 420–440 nm irradiation.²⁰ Moreover, the composition-dependent band gap of this nonisovalent solid solution enables the further optimization of its water-splitting performance by simply tuning the alloy fraction. But, experimental and theoretical studies^{21–28} report both quadratic bowing^{22,23,25,29} and linear decrease^{21,24,26–28} of the band gap with increasing ZnO content, predicting differing minimum band gaps for $(\text{Ga}_{1-x}\text{Zn}_x)(\text{N}_{1-x}\text{O}_x)$ at diverse ZnO concentrations. Meanwhile, the origin of the band-gap reduction in $(\text{Ga}_{1-x}\text{Zn}_x)(\text{N}_{1-x}\text{O}_x)$ compared with the two parent materials (GaN, ~3.4 eV, and ZnO, ~3.2 eV) is also under intense debate, and a number of different theories have been put forward, varying from *p-d* repulsion,^{21,23} through Zn impurity levels,^{30,31} to volume deformation and structural relaxation.²³ These controversies, which have caused great confusion about how to tailor the properties of this quaternary alloy, in principle, should be correlated with the uncertainty of the arrangement of the constitute elements at the atomic scale.³² A tentative theoretical mechanism, in which different degrees of short-range order (SRO), i.e., a clustering tendency to enhance the statistical presence of the valence-matched Ga-N and Zn-O pairs, account for the discrepancy in the band gaps of $(\text{Ga}_{1-x}\text{Zn}_x)(\text{N}_{1-x}\text{O}_x)$, has been proposed.^{25,28,32} This seems reasonable, but convincing experimental support for the presence of SRO is yet to emerge.

The establishment of a clear composition-structure-property relationship for $(\text{Ga}_{1-x}\text{Zn}_x)(\text{N}_{1-x}\text{O}_x)$ requires a series of geometrically well-defined single-crystal samples with fully tunable alloy fraction ($0 < x < 1$). The conventional route for synthesizing $(\text{Ga}_{1-x}\text{Zn}_x)(\text{N}_{1-x}\text{O}_x)$ solid solutions^{15,16,18,29,33} consists of nitriding mixed oxide precursors under an ammonia atmosphere for tens of hours at a high temperature (~900°C). The resulting irregularly shaped microparticles are generally limited by a low ZnO concentration and exhibit an observable nonuniform distribution of the constituent atoms, owing to the formation of an intermediate, ZnGa_2O_4 , which imposes a limit on the Zn content ($x < 0.33$),³⁴ and the volatilization of the Zn species in the presence of ammonia at high temperatures, which leads to the further removal of Zn and O atoms from the alloy.¹⁸ Recently, great efforts have been devoted to growing $(\text{Ga}_{1-x}\text{Zn}_x)(\text{N}_{1-x}\text{O}_x)$ nanocrystals because they can accommodate large lattice distortions, contributing to a much higher solubility of ZnO.³⁵ For instance, Zn-rich $(\text{Ga}_{1-x}\text{Zn}_x)(\text{N}_{1-x}\text{O}_x)$ ($x > 0.9$) nanocrystals were synthesized by nitriding a Zn-rich mixture of ZnGa_2O_4 and ZnO nanocrystals²⁴ or Ga-Zn layered double hydroxides²⁷ at relatively low temperatures (600°C–800°C). However, the downside of these methods is that solid solutions with different compositions exhibit different average particle sizes and distinct crystallinities, due to the various temperatures and/or durations used in the nitridation reactions. Nanostructured $(\text{Ga}_{1-x}\text{Zn}_x)(\text{N}_{1-x}\text{O}_x)$ with well-defined geometries, including nanowires,^{36,37} nanotubes,³⁸ polycrystalline hollow nanospheres,²⁶ and hexagonal nanosheets,³⁹ have also been reported. Nonetheless, their prospects for investigating the composition-structure-property relationship are severely restricted by either the limited alloy fraction or poor crystallinity. Therefore, the synthesis of full-composition-tunable single-crystal $(\text{Ga}_{1-x}\text{Zn}_x)(\text{N}_{1-x}\text{O}_x)$ with a well-defined geometry remains a great challenge for obtaining an in-depth understanding of the mechanism underlying the band-gap variation in this nonisovalent alloy system.

In this work, we report the synthesis of well-defined single-crystal $(\text{Ga}_{1-x}\text{Zn}_x)(\text{N}_{1-x}\text{O}_x)$ solid-solution nanowires over the full composition range ($0 < x < 1$) via a simple and effective reactor design using the chemical vapor deposition (CVD) growth strategy. X-ray absorption fine-structure analysis in combination with *ab initio* multiple-scattering calculation

¹Chinese Academy of Sciences (CAS) Center for Excellence in Nanoscience, CAS Key Laboratory of Nanosystem and Hierarchy Fabrication, National Center for Nanoscience and Technology, Beijing 100190, China

²School of Energy and Power Engineering, Nanjing University of Aeronautics and Astronautics, Nanjing 210016, China

³Beijing Synchrotron Radiation Facility, Institute of High Energy Physics, CAS, Beijing 100049, China

⁴University of CAS, Beijing 100049, China

⁵Chemical Engineering and Technology, School of Environmental Science and Engineering, and Key Laboratory of Subsurface Hydrology and Ecological Effects in Arid Region, Ministry of Education, Chang'an University, Xi'an 710064, China

⁶These authors contributed equally

⁷Lead contact

*Correspondence: jzhang@ihep.ac.cn (J.Z.), ymxuan@nuaa.edu.cn (Y.X.), gongjr@nanoctr.cn (J.R.G.)

<https://doi.org/10.1016/j.matt.2020.12.024>

verifies the existence of a strong SRO, i.e., a clustering tendency to enhance the statistical preference of the valence-matched Ga-N and Zn-O pairs, in the synthesized nanowires. This clustering effect causes the formation of intracrystalline heterojunctions between the incorporated clusters and the host material with a type II band alignment, thereby resulting in a continuous decrease in the band gap with increasing ZnO content and making the sample with the highest ZnO content exhibit the highest water-splitting activity. Our work highlights the vital role of atomic arrangement engineering in modulating the electronic band structures of nonisovalent semiconductor alloys at the atomic scale.

RESULTS AND DISCUSSION

Growth of $(\text{Ga}_{1-x}\text{Zn}_x)(\text{N}_{1-x}\text{O}_x)$ nanowires

$(\text{Ga}_{1-x}\text{Zn}_x)(\text{N}_{1-x}\text{O}_x)$ nanowires were synthesized using a customized CVD experimental setup (Figure 1A). A small quartz tube closed at one end was placed inside a horizontal, two-zone tube furnace, with the closed end of the tube facing the gas inlet, to maintain the high vapor concentration necessary for nanowire growth. Well-mixed commercial GaN, Ga_2O_3 , and ZnO powders were used as the Ga, Zn, O, and N sources, and put into a quartz boat placed at the closed end of the small quartz tube. A Si (111) slice coated with Au catalyst islands was located downstream of the precursor as the growth substrate. In between the precursors and the substrate, a second small quartz boat filled with a mixture of ZnO and graphite powder⁴⁰ was introduced to provide a Zn-rich environment. The nanowires grew in an argon-ammonia (Ar-NH₃) carrier gas mixture when the temperature of the quartz boat loaded with the GaN, Ga_2O_3 , and ZnO mixture reached 1,140°C and that of the substrate reached ~840°C (Figure 1A). In this process, commercially available powder reagents are used as precursors without lengthy pretreatment,^{41–44} and the nanowire growth is complete in 20 min, in contrast to the procedure duration of hours or even days of solid-state nitridation reactions reported in the literature.^{26,29,36,44} Moreover, the chemical composition can be continuously tuned simply by varying the component proportions of GaN, Ga_2O_3 , and ZnO in the precursor mixture without changing any other experimental parameter, ensuring the growth of $(\text{Ga}_{1-x}\text{Zn}_x)(\text{N}_{1-x}\text{O}_x)$ nanowires with complete composition tunability under identical reaction conditions.

Photos of the samples obtained at different proportions of precursor components are shown in Figure 1B. Uniform and dense thin films can be found on the Si substrates, while the color of the films changes gradually from pale gray to corn yellow with increasing ZnO content in the precursors, implying a decrease in the band gap of the samples.¹⁸ The scanning electron microscopy (SEM) images in Figure 1C demonstrate the nanowire morphology for all the samples, with average diameters varying between 40 and 100 nm and lengths in the range of 1–3 μm. Photos and SEM images of both ZnO and GaN nanowires are also given for comparison. The energy-dispersive X-ray spectroscopy (EDS) analysis results verify the existence of Zn, Ga, N, and O elements in all the synthesized nanowires (Table 1 and Figure S1). As a semiquantitative measurement, EDS is primarily used to calculate the relative ratios of Zn to Ga + Zn of the samples synthesized in this work. Accordingly, the chemical formula of these nanowires can be expressed in the form of $(\text{Ga}_{1-x}\text{Zn}_x)(\text{N}_{1-x}\text{O}_x)$ (here x represents the relative atomic ratio of Zn to Ga + Zn), with x varying from 0.18 to 0.35, 0.50, 0.68, and 0.84. The high solubility of ZnO in our $(\text{Ga}_{1-x}\text{Zn}_x)(\text{N}_{1-x}\text{O}_x)$ nanowires compared with that of the $(\text{Ga}_{1-x}\text{Zn}_x)(\text{N}_{1-x}\text{O}_x)$ synthesized via solid-state nitridation reactions can be attributed to the relatively low growth temperature (~840°C) and short growth time (~20 min), both of which restrain the volatilization of Zn.^{29,33,45} Furthermore, the excess ZnO in the precursors of both quartz boats (to compensate for the Zn loss) and the large tolerance of nanowires to lattice distortion³⁵ also favor the high content of ZnO in the nanowires.^{20,22,24,34,44}

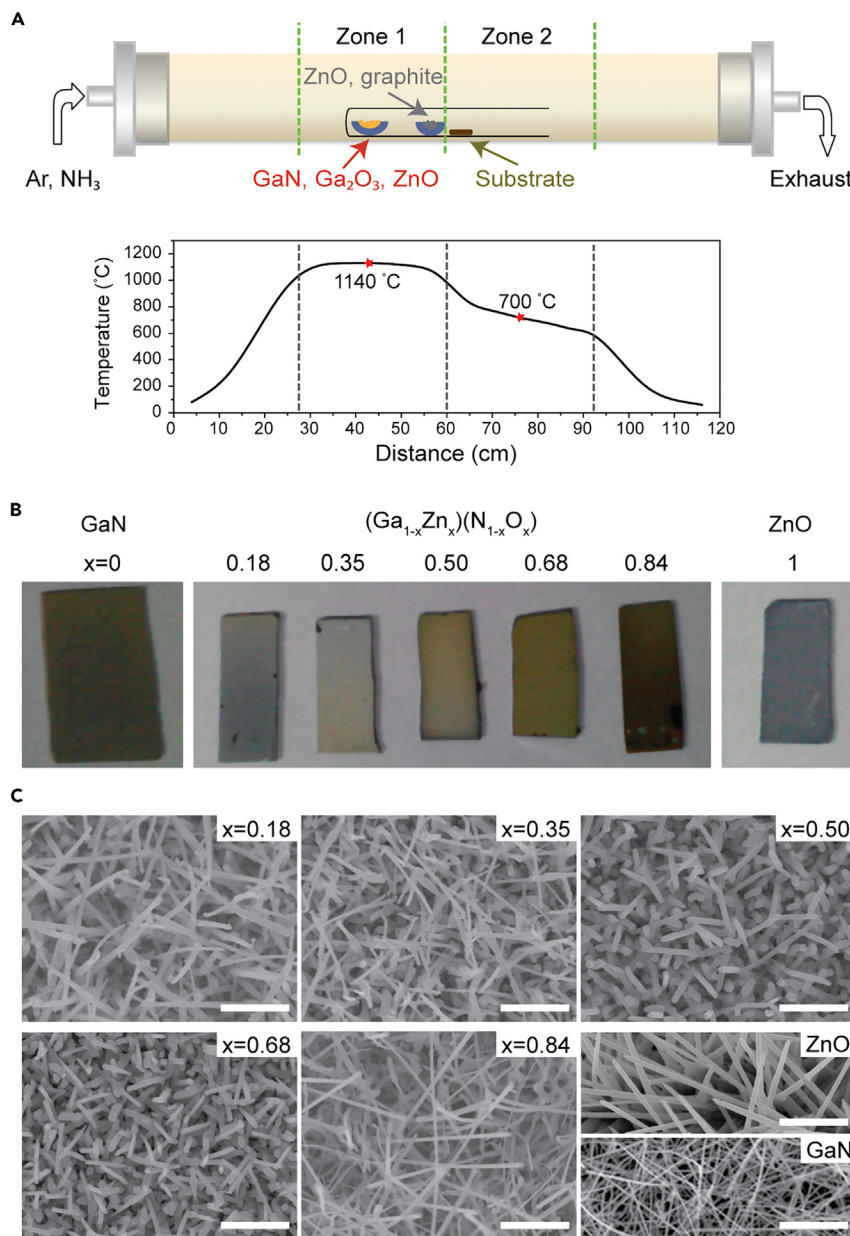


Figure 1. Growth and morphology of $(\text{Ga}_{1-x}\text{Zn}_x)(\text{N}_{1-x}\text{O}_x)$ solid-solution nanowires

(A) Experimental setup. A two-zone tube furnace is used for the CVD reaction, with two separate heating zones. The first zone is heated to 1,140°C for the evaporation of the precursors, whereas the second zone is heated to only 700°C for nanowire growth. The reactor consists of an outer horizontal quartz tube and a smaller inner one closed at one end. The Ar-NH₃ gas mixture flowing from the left side of the tube furnace functions as the precursor-vapor carrier.

(B and C) Photographs (B) and SEM images (C) of $(\text{Ga}_{1-x}\text{Zn}_x)(\text{N}_{1-x}\text{O}_x)$ nanowires ($x = 0.18, 0.35, 0.50, 0.68$, and 0.84), ZnO, and GaN on Si substrates. The size of the GaN sample is about $2 \times 1 \text{ cm}^2$, while the others are each $0.5 \times 1.5 \text{ cm}^2$. All scale bars, 1 μm.

Crystal structures of $(\text{Ga}_{1-x}\text{Zn}_x)(\text{N}_{1-x}\text{O}_x)$ nanowires and their elemental distributions

To verify the formation of solid solutions, the crystal structures and elemental distributions of $(\text{Ga}_{1-x}\text{Zn}_x)(\text{N}_{1-x}\text{O}_x)$ nanowires were investigated using different characterization techniques. X-ray diffraction (XRD) patterns (Figure 2A) show that

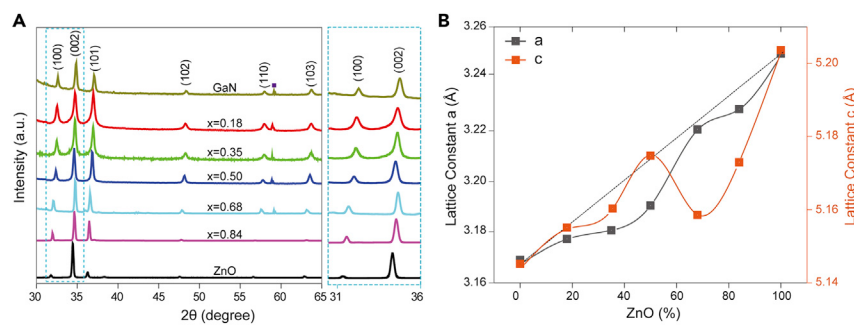
Table 1. Elemental composition, band gap, and hydrogen evolution rate of $(\text{Ga}_{1-x}\text{Zn}_x)(\text{N}_{1-x}\text{O}_x)$ nanowires

$(\text{Ga}_{1-x}\text{Zn}_x)(\text{N}_{1-x}\text{O}_x)$ nanowire	Elements (atom %)				E_g (eV) ^a	Hydrogen evolution rate ($\mu\text{mol h}^{-1}\text{cm}^{-2}$)
	Zn	Ga	N	O		
$(\text{Ga}_{0.82}\text{Zn}_{0.18})(\text{N}_{0.82}\text{O}_{0.18})$	8.98	38.74	29.87	22.40	3.02 ± 0.04	0.58 ± 0.06
$(\text{Ga}_{0.65}\text{Zn}_{0.35})(\text{N}_{0.65}\text{O}_{0.35})$	16.21	29.73	23.80	30.26	2.88 ± 0.02	0.84 ± 0.08
$(\text{Ga}_{0.50}\text{Zn}_{0.50})(\text{N}_{0.50}\text{O}_{0.50})$	21.76	21.99	23.15	33.10	2.80 ± 0.03	0.89 ± 0.09
$(\text{Ga}_{0.32}\text{Zn}_{0.68})(\text{N}_{0.32}\text{O}_{0.68})$	31.77	15.18	15.81	37.24	2.68 ± 0.02	1.39 ± 0.14
$(\text{Ga}_{0.16}\text{Zn}_{0.84})(\text{N}_{0.16}\text{O}_{0.84})$	35.28	6.49	9.02	49.21	2.59 ± 0.02	2.12 ± 0.21

^aSee the specific band-gap (E_g) calculation under Experimental procedures.

a well-crystallized single hexagonal wurtzite phase similar to those of pure GaN and ZnO is obtained for all the $(\text{Ga}_{1-x}\text{Zn}_x)(\text{N}_{1-x}\text{O}_x)$ nanowire samples. The magnified view shows that the (100) and (002) diffraction peaks are in between the corresponding peaks for pure GaN and ZnO,²² and the (100) and (002) peaks shift to lower angles with increasing x because Zn^{2+} (0.74 Å) has a larger ionic radius than Ga^{3+} (0.61 Å).²⁹ These features demonstrate that the $(\text{Ga}_{1-x}\text{Zn}_x)(\text{N}_{1-x}\text{O}_x)$ samples are not physical mixtures of GaN and ZnO, but rather solid solutions of the two constituent compounds.^{17,18,44} The lattice constants a and c (calculated from the positions of the (100) and (002) XRD peaks, respectively, and plotted as a function of the ZnO concentration in Figure 2B) deviate from the ideal solid-solution behavior described by Vegard's law,⁴⁶ and the larger deviation of c from the linear relationship compared with that of a should be attributed to the small lattice mismatch between GaN and ZnO along the c axis (0.3%) compared with that along the a axis (1.7%).^{29,37} In addition, the downward bowing of a and the fluctuation of c indicate the shrinkage of the crystal lattice in our synthesized nanowires, which is in contrast to the lattice expansion seen in most previous reports.^{22–25,28} This might be correlated with the presence of an ordered structure, as greater disorder generally causes the lattice parameters to increase.^{25,28}

The crystallinity and elemental distribution in the $(\text{Ga}_{1-x}\text{Zn}_x)(\text{N}_{1-x}\text{O}_x)$ solid-solution nanowires were examined by using transmission electron microscopy (TEM) and EDS element mapping and line-scan profiling. The smooth surface and the presence of a gold nanoparticle at the tip of a nanowire in the representative TEM image

**Figure 2.** Crystal structures of $(\text{Ga}_{1-x}\text{Zn}_x)(\text{N}_{1-x}\text{O}_x)$ solid-solution nanowires

(A) XRD patterns of $(\text{Ga}_{1-x}\text{Zn}_x)(\text{N}_{1-x}\text{O}_x)$ solid solutions and ZnO and GaN nanowires. The magnified view in the blue dashed box shows the shift of the (100) and (002) diffraction peaks with increasing x . The purple square indicates the diffraction peak from the Si substrate.

(B) Lattice constants a and c calculated from the positions of the (100) and (002) diffraction peaks, respectively.

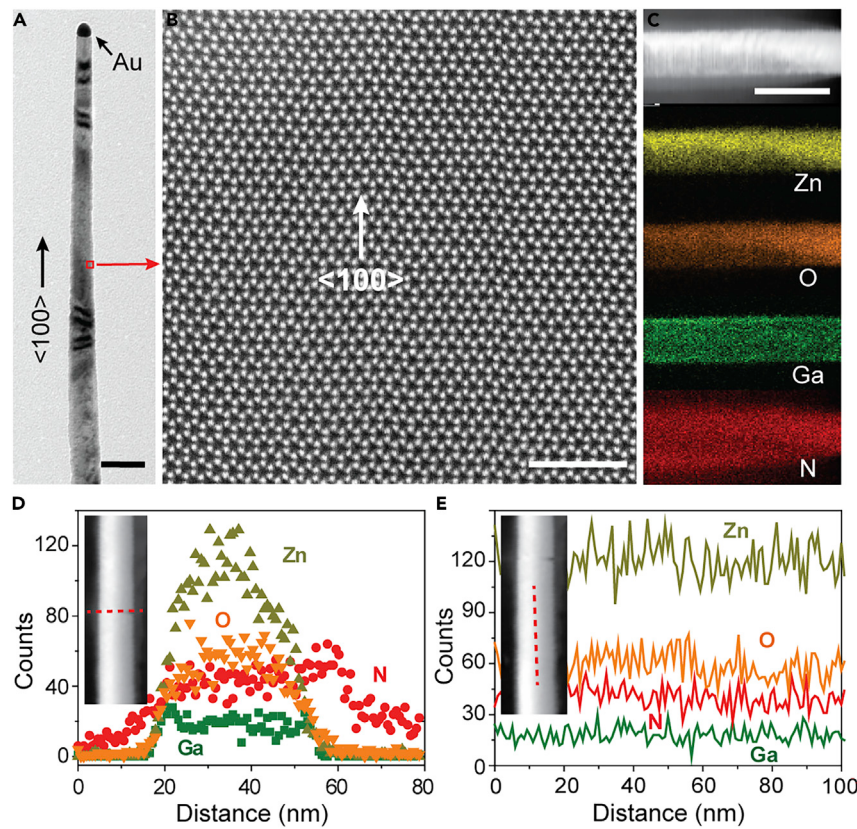


Figure 3. Crystallinity and elemental distribution in a ZnO-rich $(\text{Ga}_{0.16}\text{Zn}_{0.84})(\text{N}_{0.16}\text{O}_{0.84})$ nanowire

(A) Low-resolution TEM image (scale bar, 100 nm).

(B) High-resolution Cs-corrected TEM image (scale bar, 2 nm) showing a zoomed-in view of (A).

(C) EDS mapping (scale bar, 50 nm) of the solid-solution nanowire.

(D and E) Line-scan profiling of Zn, O, Ga, and N elements across (D) and along (E) the nanowire, as indicated by the red dashed lines in the insets.

(Figure 3A) confirm the vapor-liquid-solid mechanism for nanowire growth.⁴⁷ The high-resolution (HR) spherical aberration-corrected TEM (Cs-corrected TEM) image (Figure 3B) reveals well-arranged atom arrays, indicating the good crystallinity of the ZnO-rich $(\text{Ga}_{0.16}\text{Zn}_{0.84})(\text{N}_{0.16}\text{O}_{0.84})$ nanowire. The HR-TEM images (Figures S2A–S2E) show that the solid-solution nanowires, irrespective of the ZnO concentration, all grew along the $<100>$ direction, with space lattices corresponding to the hexagonal wurtzite structure. Moreover, the lattice fringes in the nanowires are regularly spaced and defect free, confirming the excellent crystal quality of the $(\text{Ga}_{1-x}\text{Zn}_x)(\text{N}_{1-x}\text{O}_x)$ nanowires.^{41,48,49} This result is further verified by the fast Fourier transform patterns, since no overlapping or splitting of diffraction spots is observed (Figures S2F–S2J). The four constituent elements, including Zn, O, Ga, and N, are homogeneously distributed across and along the ZnO-rich nanowire at the nanoscale, according to the EDS element mapping (Figure 3C and Table S1) and line-scan profiling (Figures 3D and 3E). That is, there is no nonuniform distribution of the constituent atoms nor phase segregation in the synthesized nanowires at the nanometer scale. Similar results were also observed for the GaN-rich $(\text{Ga}_{0.67}\text{Zn}_{0.33})(\text{N}_{0.67}\text{O}_{0.33})$ nanowires (Figure S3 and Table S1). Therefore, $(\text{Ga}_{1-x}\text{Zn}_x)(\text{N}_{1-x}\text{O}_x)$ single-crystal nanowires with complete composition tunability have been successfully synthesized, which would be promising for the further investigation of the local atomic structure of these nonisovalent alloys.

Short-range order in $(\text{Ga}_{1-x}\text{Zn}_x)(\text{N}_{1-x}\text{O}_x)$

The atomic-scale multiple element distribution in a solid solution is a characteristic structural “degree of freedom” in multiple element alloys, which plays a decisive role in controlling the physical, chemical, electronic, and mechanical properties of the material.^{13,14} Hence, a thorough investigation of the local atomic structure of $(\text{Ga}_{1-x}\text{Zn}_x)(\text{N}_{1-x}\text{O}_x)$ is a prerequisite for further understanding of its functional properties. In our case, the consistent wurtzite crystal structure and the uniform distribution of constituent elements at the nanometer scale in the $(\text{Ga}_{1-x}\text{Zn}_x)(\text{N}_{1-x}\text{O}_x)$ solid-solution nanowires were shown by TEM and EDS analysis. But these techniques do not provide sufficient information to determine whether the alloys are ordered or disordered at the atomic scale.³² Nonetheless, the lattice constant of short-range ordered $(\text{Ga}_{1-x}\text{Zn}_x)(\text{N}_{1-x}\text{O}_x)$ has been reported to be smaller than that of the disordered alloy.²⁸ That is, the shrinkage of the crystal lattice in our solid solutions might imply the existence of SRO (Figure 2B). To verify this inference, we employed X-ray absorption near-edge structure (XANES) spectroscopy to investigate the local structures of Ga and Zn sites because the main effect of SRO is to enhance the statistical presence of the valence-matched Ga-N and Zn-O pairs,^{25,28,32} and the finer details of these nearest-neighbor bondings have been reported to appear as differences in the precise edge shape of XANES spectra.^{50–52} The K-edge XANES data reveal that the local structures around Ga and Zn atoms in $(\text{Ga}_{1-x}\text{Zn}_x)(\text{N}_{1-x}\text{O}_x)$ are similar to those in the GaN and ZnO nanowires (Figures 4A and 4D). This observation verifies the tetrahedral coordination environments of Ga and Zn atoms in the wurtzite crystal structure.^{22,45} A closer look at the XANES spectra shows that the shoulder peak A in front of the corresponding main absorption peak B at the Ga K-edge of $(\text{Ga}_{1-x}\text{Zn}_x)(\text{N}_{1-x}\text{O}_x)$ (Figure 4A) seems to be stronger than that of the GaN nanowire, whereas peak A at the Zn K-edge of $(\text{Ga}_{1-x}\text{Zn}_x)(\text{N}_{1-x}\text{O}_x)$ is slightly weaker than that in the ZnO nanowire (Figure 4D). Moreover, the intensity of peak A at the Ga K-edge of $(\text{Ga}_{1-x}\text{Zn}_x)(\text{N}_{1-x}\text{O}_x)$ decreases with increasing x , and peak D₃ in the tail of positive peak D gradually disappears at the Zn K-edges.^{53,54} The alterations in these feature peaks, which are sensitive to small variations in the local structure, might be correlated with the existence of SRO in $(\text{Ga}_{1-x}\text{Zn}_x)(\text{N}_{1-x}\text{O}_x)$, but have been rarely investigated in previous reports.

To correlate the above changes in the XANES spectra with the existence of SRO in $(\text{Ga}_{1-x}\text{Zn}_x)(\text{N}_{1-x}\text{O}_x)$, *ab initio* multiple-scattering calculations of XANES spectra, which are effective in uncovering the local atomic configuration,^{50,51} were performed at the Ga and Zn K-edges of two different model systems. First, we calculated the XANES spectra at the Ga and Zn K-edges of the GaN, ZnO, GaO, and ZnN unit cells with the same wurtzite structure (Figures S4A, S4G, S5A, and S5G).⁵⁵ The coordination environments of the Ga and Zn atoms in the GaN and ZnO unit cells under the extreme conditions of $x = 0$ and 1 can be considered to be analogous to those of the atoms in short-range ordered $(\text{Ga}_{1-x}\text{Zn}_x)(\text{N}_{1-x}\text{O}_x)$ ($0 < x < 1$), considering their valence-matched Ga-N and Zn-O bonding pairs.^{25,28} In contrast, the coordination environments of the Ga and Zn atoms in GaO and ZnN should be similar to those of the atoms in disordered $(\text{Ga}_{1-x}\text{Zn}_x)(\text{N}_{1-x}\text{O}_x)$, in which the nonmetal atoms coordinated to Ga and Zn are all O and N atoms, respectively. For the simulated Ga K-edge spectra of GaN and GaO (Figure 4B), the most prominent change caused by the substitution of N with O atoms is the disappearance of shoulder peak A. Conversely, the replacement of O with N atoms leads to a remarkable increase in the intensity of peak A at the Zn K-edge spectrum of ZnN compared with that of ZnO (Figure 4E). For more quantitative discussion, first derivative computations were performed on the calculated XANES spectra (Figures S6A and S6C). The emerging of peak A in XANES spectra is found to cause a drastic fluctuation in its

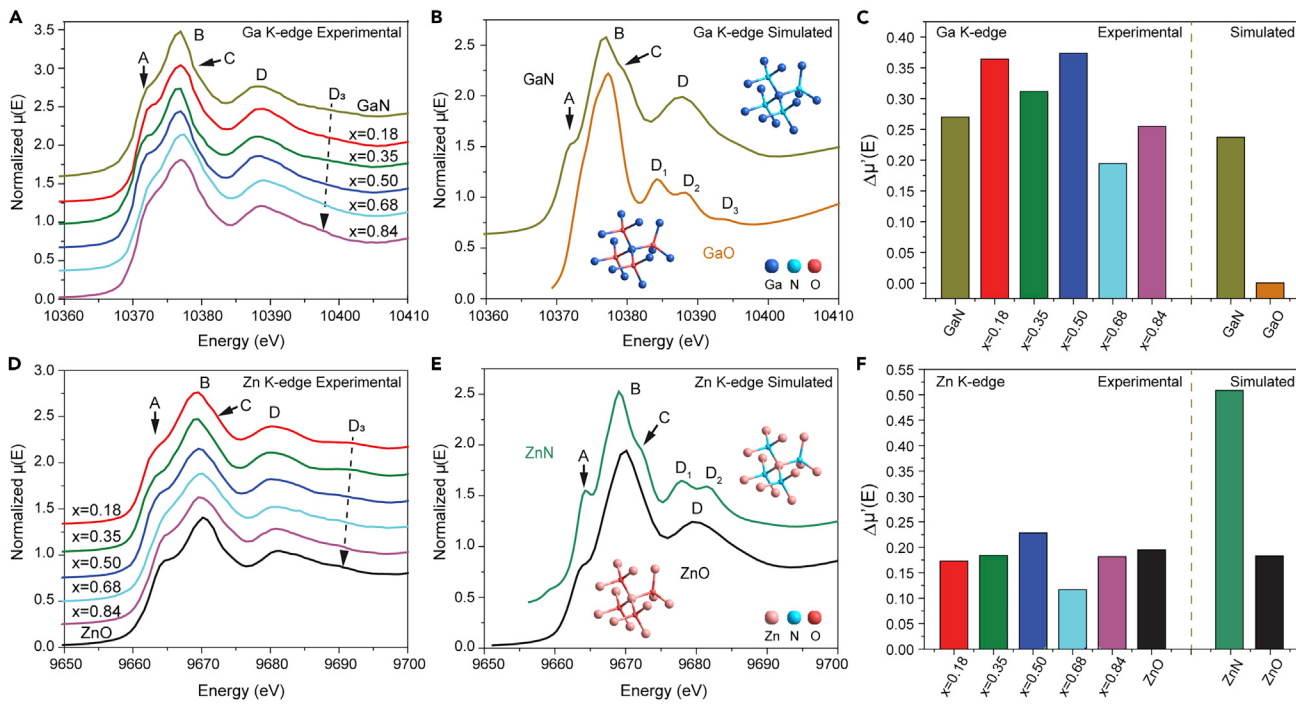


Figure 4. Local structure characterization of $(\text{Ga}_{1-x}\text{Zn}_x)(\text{N}_{1-x}\text{O}_x)$ by XANES spectroscopy

(A and D) Normalized XANES spectra at the Ga (A) and Zn (D) K-edges for various x values ($x = 0.18, 0.35, 0.50, 0.68$, and 0.84). Pure ZnO and GaN nanowires are used as references.

(B and E) Computational XANES spectra for GaN and GaO at the Ga K-edge (B) and ZnO and ZnN at the Zn K-edge (E), with the insets showing the coordination environments around the central Ga and Zn atoms.

(C and F) The difference between the maximum and the minimum values of the first derivative XANES spectra of $(\text{Ga}_{1-x}\text{Zn}_x)(\text{N}_{1-x}\text{O}_x)$ in the energy range of 10,369–10,374 eV and 9,661–9,666 eV for the Ga (C) and Zn (F) K-edges, respectively.

$\mu(E)$ represents the X-ray absorption coefficient of the sample.

first derivative (the light blue region in Figures S6A and S6C), and the difference between the maximum and the minimum values of the first derivative ($\Delta\mu'(E)$) can be used to quantitatively describe the change in the intensity of peak A. For instance, the substantial decrease in the value of $\Delta\mu'(E)$ at the Ga K-edge after the substitution of N with O atoms (Figure 4C) corresponds to the significant reduction in the intensity of peak A (Figure 4B), while the much higher $\Delta\mu'(E)$ at the Zn K-edge of ZnN compared with that of the ZnO (Figure 4F) coincides with the remarkable reinforcement in the peak intensity (Figure 4E). We also calculated the first derivative XANES spectra of the synthesized GaN, $(\text{Ga}_{1-x}\text{Zn}_x)(\text{N}_{1-x}\text{O}_x)$, and ZnO nanowires (Figures S6B and S6D) as well as the values of $\Delta\mu'(E)$ (Figures 4C and 4F). The values of $\Delta\mu'(E)$ at the Ga K-edge spectra of $(\text{Ga}_{1-x}\text{Zn}_x)(\text{N}_{1-x}\text{O}_x)$ nanowires are stronger than or comparable to that of the GaN nanowire, in distinct contrast to the near-zero $\Delta\mu'(E)$ value of the GaO, implying the low substitution ratio of N with O around Ga atoms. Likewise, the slightly smaller values of $\Delta\mu'(E)$ at the Zn K-edge spectra of $(\text{Ga}_{1-x}\text{Zn}_x)(\text{N}_{1-x}\text{O}_x)$ nanowires compared with that of the ZnO nanowire also imply well-preserved Zn-O coordination environments, because the substitution of O with N around Zn atoms has been proven to cause a sharp increase in the value of $\Delta\mu'(E)$. Thus, the presence of SRO in $(\text{Ga}_{1-x}\text{Zn}_x)(\text{N}_{1-x}\text{O}_x)$ nanowires is validated by comparing the intensity of peak A at both the Ga and the Zn K-edges in the experimental XANES spectra of $(\text{Ga}_{1-x}\text{Zn}_x)(\text{N}_{1-x}\text{O}_x)$ with those of GaN and ZnO. In addition, the decrease in the intensity of peak A with increasing x at the Ga K-edge (Figure 4A) could be attributed to the increasing number of Ga-O bonds at higher ZnO concentrations, and the reason

for the increase in the intensity of peak D₃ located at the energy range from 9,685 to 9,695 eV in the Zn K-edge XANES spectra with decreasing x in [Figure 4D](#) should be related to the formation of more Zn-N bonds in the GaN host structure. This is evident from the similar shape of the first derivative XANES curve of ZnN and low ZnO concentration ($\text{Ga}_{1-x}\text{Zn}_x(\text{N}_{1-x}\text{O}_x)$) nanowires (x < 0.50) in this energy region ([Figures S6C](#) and [S6D](#)). This is reasonable, as the component elements in these nanowires distribute uniformly at the nanometer scale; thus, the statistical presence of valence-mismatched Ga-O (Zn-N) bonding will certainly increase at high (low) ZnO concentrations.

Nonetheless, only the effect of the nearest-neighbor bondings on the precise shape of XANES spectra can be reflected by using the above model unit cells, wherein the roles of the cation and anion sublattice configurations in the wurtzite structure are not included. Thus, XANES calculations were further performed on short-range ordered and disordered ($\text{Ga}_{1-x}\text{Zn}_x(\text{N}_{1-x}\text{O}_x)$) supercell models, i.e., the special quasi-ordered (SQoS) and quasi-disordered (SQdS) structures reported by Liu et al.,²⁸ which have compositions close to those of our experimental samples ([Figures S4](#) and [S5](#)). Peak A in all the computed curves of SQoS ($\text{Ga}_{1-x}\text{Zn}_x(\text{N}_{1-x}\text{O}_x)$) at both the Ga and the Zn K-edges ([Figures S7A](#) and [S7D](#)) reproduces the corresponding changes in the experimental spectra well ([Figures 4A](#) and [4D](#)), wherein the values of $\Delta\mu'(\text{E})$ at the Ga K-edge spectra when x ≤ 0.5 are comparable to that of the GaN ([Figure S7C](#)), and the $\Delta\mu'(\text{E})$ values at the Zn K-edge are all close to that of the ZnO ([Figure S7F](#)). As for the slightly lower $\Delta\mu'(\text{E})$ at high ZnO content, it could be attributed to the increasing number of Ga-O bonds ([Figure S7C](#)). In contrast, the much smaller values of $\Delta\mu'(\text{E})$ at the Ga K-edge of SQdS ($\text{Ga}_{1-x}\text{Zn}_x(\text{N}_{1-x}\text{O}_x)$) compared with that of the GaN ([Figures S7B](#) and [S7C](#)) imply the weaker intensity of peak A, and peak A in the Zn K-edge spectra of SQdS ($\text{Ga}_{1-x}\text{Zn}_x(\text{N}_{1-x}\text{O}_x)$) is more salient than that in ZnO according to the higher $\Delta\mu'(\text{E})$ values ([Figures S7E](#) and [S7F](#)); both these results are inconsistent with the changes in our experimental spectra. Furthermore, the calculated spectra of SQoS ($\text{Ga}_{1-x}\text{Zn}_x(\text{N}_{1-x}\text{O}_x)$) ([Figure S7D](#)) also reproduce the gradual decrease in peak D₃ with increasing x ([Figure 4D](#)) at the Zn K-edge, whereas such similarity cannot be found in the spectra of SQdS ($\text{Ga}_{1-x}\text{Zn}_x(\text{N}_{1-x}\text{O}_x)$) ([Figure S7E](#)). These calculations at the atomic scale further support the presence of SRO in the synthesized ($\text{Ga}_{1-x}\text{Zn}_x(\text{N}_{1-x}\text{O}_x)$) nanowires. In addition, the XANES simulation results for SQoS ($\text{Ga}_{0.5}\text{Zn}_{0.5}(\text{N}_{0.5}\text{O}_{0.5})$) show that the intensity of peak A is associated with the scattering contributions of coordination shells within a distance up to 0.7 nm from the center atom's base ([Figure S8](#)). This is the reason imaging inhomogeneity or clusters via electron microscopy for an unambiguous description of the atomic arrangement within the lattice has historically been difficult.

Band-gap variation in ($\text{Ga}_{1-x}\text{Zn}_x(\text{N}_{1-x}\text{O}_x)$)

SRO has been reported to significantly influence the energy band structures of ($\text{Ga}_{1-x}\text{Zn}_x(\text{N}_{1-x}\text{O}_x)$) solid solutions;²⁸ these energy bands are closely associated with their performance in overall water splitting. Hence, the specific band gaps of our samples were calculated from the absorption onsets and Tauc plots obtained from the normalized UV-visible (UV-vis) diffuse reflectance spectra ([Figures S9](#) and [S10](#)).⁴⁸ The relative absorbance spectra obtained from the Kubelka-Munk transform of the reflectance data ([Figure 5A](#)) show that the absorption onset of ($\text{Ga}_{1-x}\text{Zn}_x(\text{N}_{1-x}\text{O}_x)$) monotonically red shifts from 410 nm at x = 0.18 to 478 nm at x = 0.84, corresponding to a change in the band gap from 3.02 to 2.59 eV ([Tables 1](#) and [S2](#)). The direct band-gap change from 3.15 to 2.66 eV calculated from the Tauc plots displays the same trend for ($\text{Ga}_{1-x}\text{Zn}_x(\text{N}_{1-x}\text{O}_x)$) ([Figure 5B](#)) with increasing x, consistent with the color change of these samples ([Figure 1B](#)). The same ZnO content-dependent band-gap trends

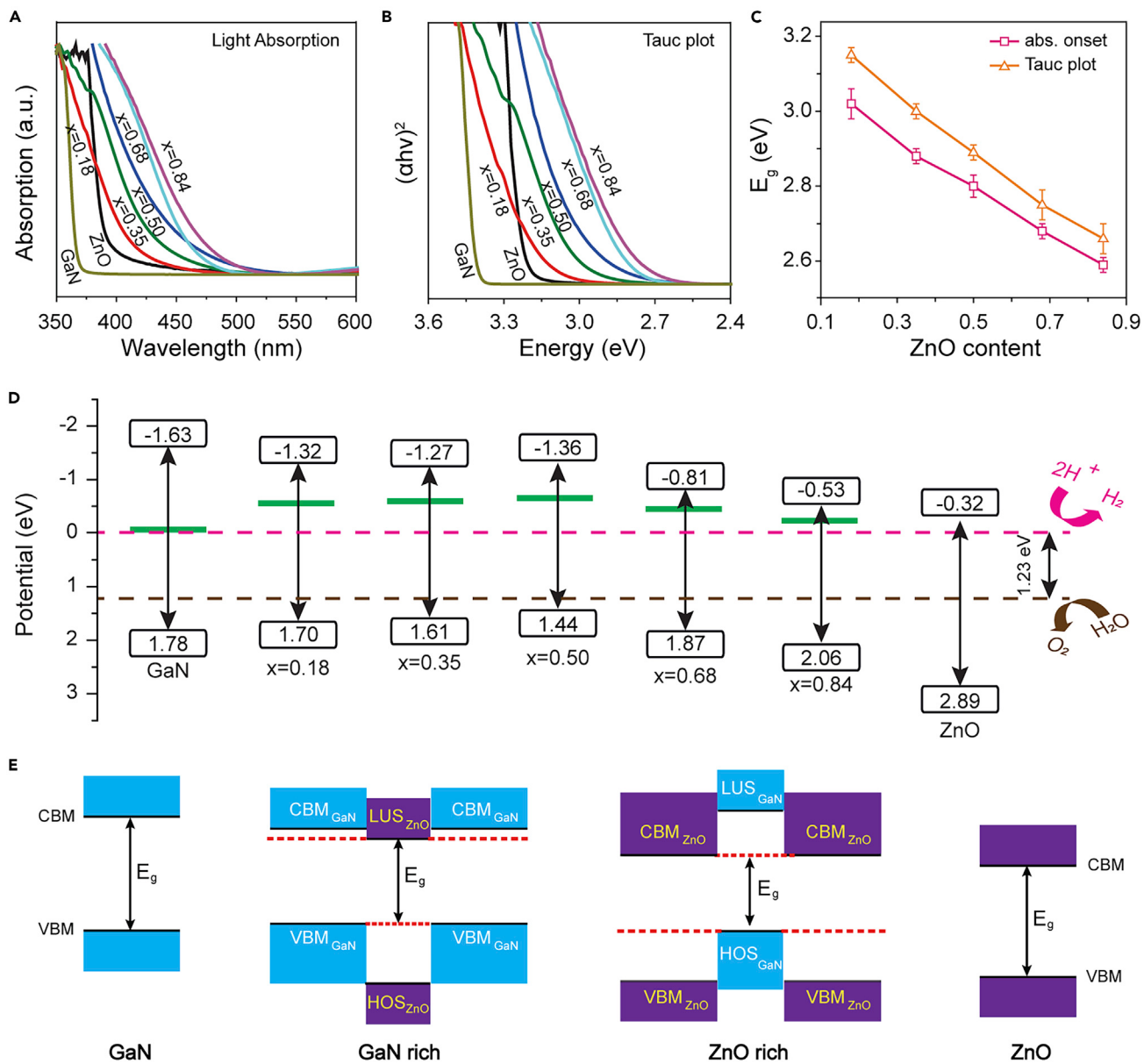


Figure 5. Band-gap change and energy band structures in $(\text{Ga}_{1-x}\text{Zn}_x)(\text{N}_{1-x}\text{O}_x)$ solid-solution nanowires

(A) Normalized UV-visible absorption spectra.

(B) Tauc plots.

(C) Summary of the ZnO content-dependent band-gap changes calculated from the absorption onsets and Tauc plots. The error bars show the mean absolute errors.

(D) Energy-level diagram of $(\text{Ga}_{1-x}\text{Zn}_x)(\text{N}_{1-x}\text{O}_x)$ ($0 < x < 1$). The work functions of $(\text{Ga}_{1-x}\text{Zn}_x)(\text{N}_{1-x}\text{O}_x)$ nanowire films are marked by green lines.

(E) Schematic diagram of the band-gap reduction mechanism in $(\text{Ga}_{1-x}\text{Zn}_x)(\text{N}_{1-x}\text{O}_x)$ solid solutions compared with their parent GaN and ZnO bulk materials, arranged from left to right in order of increasing x from 0 to 1. LUS, lowest unoccupied state; HOS, highest occupied state. Pure ZnO and GaN are used as reference samples in (A), (D), and (E).

obtained from these spectra (Figure 5C) clearly demonstrate a continuous decrease in the band gap of $(\text{Ga}_{1-x}\text{Zn}_x)(\text{N}_{1-x}\text{O}_x)$ with increasing x . These results are strongly supported by the calculation results for the short-range ordered $(\text{Ga}_{1-x}\text{Zn}_x)(\text{N}_{1-x}\text{O}_x)$.²⁸ Moreover, the band gaps of our $(\text{Ga}_{1-x}\text{Zn}_x)(\text{N}_{1-x}\text{O}_x)$ nanowires are much larger than those of the reported $(\text{Ga}_{1-x}\text{Zn}_x)(\text{N}_{1-x}\text{O}_x)$ powders. This could be attributed to the high degree of SRO in the synthesized nanowires.²⁸

Relationship between SRO and the energy band structure of $(\text{Ga}_{1-x}\text{Zn}_x)(\text{N}_{1-x}\text{O}_x)$

To explore the intrinsic mechanism of the band-gap reduction, we first measured the band-edge energy levels of the $(\text{Ga}_{1-x}\text{Zn}_x)(\text{N}_{1-x}\text{O}_x)$ solid-solution nanowires. The work function and the valence band maximum (VBM) were obtained via UV photo-electron spectroscopy (UPS) (Figure S11), while the conduction band minimum (CBM) was calculated by subtracting the band-gap energy from the VBM (Figure S12). Figure 5D depicts the energy level diagrams of the $(\text{Ga}_{1-x}\text{Zn}_x)(\text{N}_{1-x}\text{O}_x)$ solid-solution nanowires with increasing x , along with those of the pure GaN nanowire and ZnO reference samples (the band-edge energy levels of ZnO were adopted from Xu and Schoonen⁵⁶). The VBM of the solid-solution nanowires shows a parabolic change with an upward bowing over the full composition range, reaching the smallest value at $x = 0.50$; while the CBM trends downward with increasing x , with a higher magnitude at higher ZnO concentration relative to the CBM of GaN. Moreover, the positions of the work functions of $(\text{Ga}_{1-x}\text{Zn}_x)(\text{N}_{1-x}\text{O}_x)$ nanowire films are also marked by green lines in Figure 5D. Apparently, the Fermi levels of $(\text{Ga}_{1-x}\text{Zn}_x)(\text{N}_{1-x}\text{O}_x)$ nanowires are all close to their CBMs, indicating the N-type conductivity, and move closer to the CBM with increasing ZnO content.

The effect of atomic arrangement on the electronic properties of III-V semiconductor alloys has been widely investigated, and the change in electronic band structure in clustering alloys has been understood by the localization of band-edge wave functions using a “quantum-well picture.”⁵⁷ Similarly, we consider that the existence of SRO effect in $(\text{Ga}_{1-x}\text{Zn}_x)(\text{N}_{1-x}\text{O}_x)$ solid-solution nanowires will induce the formation of intracrystalline heterojunctions between the incorporated clusters and the host material at each specific x value, i.e., valence-matched Zn-O or Ga-N clusters randomly dispersed in a wurtzite structured GaN or ZnO host crystal (Figure 5E).^{21,32} Owing to the type II band offset between the bulk GaN and the bulk ZnO, the CBM and VBM of these intracrystalline heterojunctions will lie in ZnO and GaN, respectively. But, owing to quantum confinement, the lowest unoccupied state (LUS) and highest occupied state (HOS) of the clusters will not be at the same positions as the CBM and VBM of their corresponding bulk material.

At a low ZnO concentration ($x < 0.5$) (Figure 5E), the confinement occurs for the unoccupied state of the Zn-O clusters when they are incorporated into the GaN host.²¹ Owing to the light CBM effective mass, the upshift of the LUS of the Zn-O clusters is large;²¹ thus, the position of the LUS of the Zn-O clusters is much higher than the CBM of the ZnO bulk and close to that of GaN. The HOS of Zn-O is usually assumed to have little effect on the VBM of GaN. As a result, the band gap is slightly reduced when the Zn-O clusters are incorporated into the GaN host. With increasing ZnO content from 0 to 0.5, the size of the Zn-O clusters continues to increase. Thus, the effect of quantum confinement on the LUS of the Zn-O clusters in the GaN host is gradually weakened, causing a continuous lowering of the CBM of $(\text{Ga}_{1-x}\text{Zn}_x)(\text{N}_{1-x}\text{O}_x)$ ($x < 0.5$). Apparently, the downshift of the CBM is the dominant factor for the band-gap reduction in the GaN-rich $(\text{Ga}_{1-x}\text{Zn}_x)(\text{N}_{1-x}\text{O}_x)$ relative to the bulk GaN (Figure 5E). At a high ZnO concentration ($x > 0.5$) (Figure 5E), the HOS of the Ga-N clusters will shift downward relative to the VBM of GaN because of the confinement from the ZnO host. However, the downward shift is small due to the heavy VBM effective mass.²¹ In addition, the LUS of the Ga-N clusters is expected to have little effect on the CBM of ZnO.²¹ Thus, the band gap is significantly reduced when the Ga-N clusters are incorporated into the ZnO host. With increasing ZnO content from 0.5 to 1, the effect of quantum confinement on the HOS of the GaN clusters in the ZnO host is gradually strengthened, thereby leading to a gradual downshift of the VBM of $(\text{Ga}_{1-x}\text{Zn}_x)(\text{N}_{1-x}\text{O}_x)$ ($x > 0.5$). In comparison with bulk ZnO, the upshift of the VBM dominates the band reduction in ZnO-rich

$(\text{Ga}_{1-x}\text{Zn}_x)(\text{N}_{1-x}\text{O}_x)$. In addition, the weak confinement effect on the CBM of the ZnO host also has a minor influence, which causes a slight change in the CBM in $(\text{Ga}_{1-x}\text{Zn}_x)(\text{N}_{1-x}\text{O}_x)$ at high ZnO content.

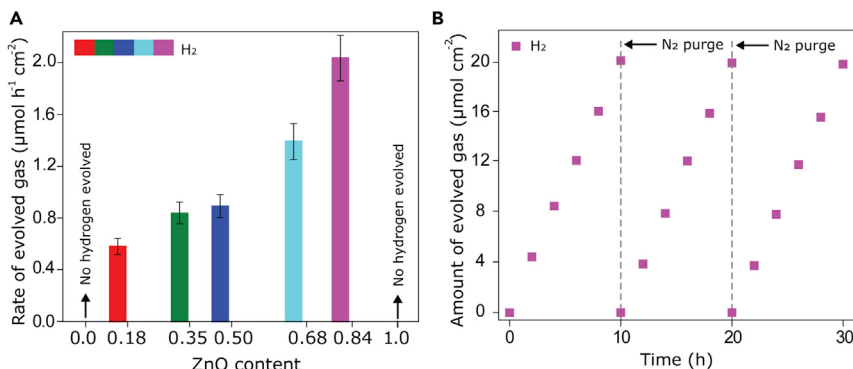
Therefore, the SRO effect plays a central role in determining the energy band structure of this nonisovalent alloy, thereby causing a linear band-gap reduction in the $(\text{Ga}_{1-x}\text{Zn}_x)(\text{N}_{1-x}\text{O}_x)$ solid-solution nanowires ($0 < x < 1$) with increasing ZnO content. In addition, the upward bowing VBM might also be correlated with the N 2p-Zn 3d repulsion in $(\text{Ga}_{1-x}\text{Zn}_x)(\text{N}_{1-x}\text{O}_x)$.^{21,23,30} Notwithstanding, the strength of the N 2p-Zn 3d repulsion will be affected by SRO, which inhibits nearest-neighbor Zn-N bonding clusters.

Water-splitting performance under visible light

We evaluated the water-splitting activities of the synthesized $(\text{Ga}_{1-x}\text{Zn}_x)(\text{N}_{1-x}\text{O}_x)$ nanowire thin films to investigate the effect of the band-gap change on their catalytic properties. The experiment was conducted under atmospheric pressure at room temperature with irradiation of visible light ($\lambda \geq 400$ nm, [Figure S13](#)), and the electrolyte was an aqueous H_2SO_4 solution at pH 4.5 without any sacrificial reagents.^{58,59} Bare $(\text{Ga}_{1-x}\text{Zn}_x)(\text{N}_{1-x}\text{O}_x)$ solid solutions can photocatalyze the water oxidation half-reaction but cannot reduce protons to generate H_2 , even in methanol solution.^{60–62} Therefore, a Rh/Cr₂O₃ core/shell cocatalyst, which has been proven to be essential for achieving overall water splitting in a $(\text{Ga}_{1-x}\text{Zn}_x)(\text{N}_{1-x}\text{O}_x)$ system, was deposited on the $(\text{Ga}_{1-x}\text{Zn}_x)(\text{N}_{1-x}\text{O}_x)$ nanowires to enable proton reduction ([Figures S14](#) and [S15](#)). All $(\text{Ga}_{1-x}\text{Zn}_x)(\text{N}_{1-x}\text{O}_x)$ nanowires were active for water splitting in the presence of the Rh/Cr₂O₃ cocatalyst and could produce H_2 without any sacrificial reagents ([Figure 6A](#) and [Table 1](#)), indicating their capability for water splitting under visible light. (Here, only the hydrogen gas evolution rate is reported because the amount of evolved oxygen cannot be accurately measured using our experimental apparatus, [Figure S16](#); and hydrogen does not originate from the Si substrate as evidenced from the chromatogram in [Figure S17](#).) This result is reasonable, as the band positions of all the synthesized nanowires straddle the water redox potentials ([Figure 5D](#)). In contrast, no activity is detected under visible light for either GaN or ZnO nanowires owing to their large band gaps, which make them unresponsive to visible light. Moreover, the water-splitting activity of the $(\text{Ga}_{1-x}\text{Zn}_x)(\text{N}_{1-x}\text{O}_x)$ nanowires monotonically increases with increasing x, reaching the highest value at $x = 0.84$. The activity change is likely due to the band-gap narrowing in $(\text{Ga}_{1-x}\text{Zn}_x)(\text{N}_{1-x}\text{O}_x)$ with increasing ZnO concentration, since the narrow band gap of the material is beneficial for sunlight-harvesting ability. The highest H_2 evolution rate of the $(\text{Ga}_{1-x}\text{Zn}_x)(\text{N}_{1-x}\text{O}_x)$ nanowire thin films is $2.12 \mu\text{mol h}^{-1} \text{cm}^{-2}$, with a corresponding light-to-hydrogen conversion efficiency of $\sim 0.06\%$, which is lower than that of the Ru-modified SrTiO₃:La,Rh/Au/BiVO₄:Mo photocatalyst sheet (0.29%) but higher than most particulate photocatalytic systems ([Table S3](#)).⁶³ Further improvement in the water-splitting performance could be expected from decreasing the background pressure, because hydrogen bubbles need higher numbers of gas molecules to desorb from the nanowires at atmospheric pressure. The stability of $(\text{Ga}_{0.16}\text{Zn}_{0.84})(\text{N}_{0.16}\text{O}_{0.84})$ nanowire thin film was also evaluated by running the photocatalytic experiment for three successive cycles during a 30 h test. No noticeable decrease in the photocatalytic activity was observed ([Figure 6B](#)), indicating the high stability of our $(\text{Ga}_{1-x}\text{Zn}_x)(\text{N}_{1-x}\text{O}_x)$ nanowires in the water-splitting reaction.

Conclusions

We synthesized a series of $(\text{Ga}_{1-x}\text{Zn}_x)(\text{N}_{1-x}\text{O}_x)$ single-crystal solid-solution nanowires over the full composition range using a customized CVD experimental setup,

**Figure 6. Water-splitting performance under visible light**

(A) Water-splitting activity of Rh/Cr₂O₃-loaded (Ga_{1-x}Zn_x)(N_{1-x}O_x) nanowires with different ZnO concentrations under visible-light irradiation. The error bars show the mean absolute errors.

Reactions were carried out under Xe lamp (300 W) illumination ($\lambda \geq 400$ nm) at room temperature and atmospheric pressure in an aqueous H₂SO₄ solution at pH 4.5.

(B) Time course of the visible-light-driven water-splitting performance of the (Ga_{0.16}Zn_{0.84})(N_{0.16}O_{0.84}) nanowires. The reaction continued for 30 h, with N₂ purging of the system every 10 h.

wherein the chemical composition was tuned by simply varying the component proportions of the precursor mixture without changing any other experimental parameter, thus ensuring the growth of nanowires with different compositions under identical reaction conditions. In accordance with recent reports, we found a continuous decrease in the band gap of (Ga_{1-x}Zn_x)(N_{1-x}O_x) with increasing ZnO content. And, the synthesized nanowires all showed excellent photocatalytic water-splitting activity for the evolution of gaseous hydrogen without any sacrificial reagents under visible-light irradiation, with the best performance being achieved by the sample with the highest ZnO content because of its smallest band gap and most favorable band positions. Considering the decisive role of atomic arrangement in controlling the mechanical, optical, electronic, and/or catalytic properties of multiple element alloys, we systematically investigated the relationship between the local atomic structures and their optical properties. Synchrotron XANES analysis in combination with *ab initio* multiple-scattering calculation verified the correlation between the finer details of the local atomic configuration and the precise edge shape of XANES spectra and the existence of SRO; i.e., a clustering tendency to enhance the statistical presence of the valence-matched Ga-N and Zn-O pairs was validated. This clustering behavior induced the formation of an intracrystalline heterojunction with a type II energy level alignment between the incorporated cluster and the host material, thereby dominating the variation in electronic band structure of (Ga_{1-x}Zn_x)(N_{1-x}O_x) with the change in composition. These findings highlight the vital role of atomic arrangement engineering in modulating the energy band structures of nonisovalent semiconductor alloys at the atomic scale. Accordingly, the discrepancy in the band gaps of (Ga_{1-x}Zn_x)(N_{1-x}O_x) materials with the same composition reported in the literature becomes reasonable with the consideration of the atomic-scale element distribution, as the discrepant thermodynamic driving forces and different atom diffusion paths for the formation of oxy(nitride) solid solutions under diverse growth conditions could lead to infinite atomic arrangement configurations, i.e., different degrees of SRO. Therefore, the atomic-scale element distribution will be a unique structural “degree of freedom” for band-gap engineering in multiple-element semiconductor alloys, greatly benefiting the development of new functional materials for energy conversion applications in future.

EXPERIMENTAL PROCEDURES

Resource availability

Lead contact

The lead contact for this article is Professor Jian Ru Gong, e-mail: gongjr@nanoctr.cn.

Materials availability

GaN (99.99%, metals basis), Ga₂O₃ (99.99%, metals basis), ZnO (99.99%, metals basis), K₂CrO₄ (ACS, 99% min), and Na₃RhCl₆ (Rh 17.1%) were purchased from Alfa Aesar. Graphite (powder, <20 µm, synthetic) was purchased from Sigma-Aldrich. H₂SO₄ (95.0%–98.0%) was obtained from Sinopharm Chemical Reagent Co., Ltd. All chemicals were purchased commercially and used without further purification. Aqueous solutions were prepared with ultrapure water (DI water; Milli-Q, 18.2 MΩ·cm).

Data availability

The data that support the findings of this study are available from the corresponding author upon reasonable request.

Nanowire synthesis

Single-crystal (Ga_{1-x}Zn_x)(N_{1-x}O_x) solid-solution nanowires were grown on the Au-coated Si (111) substrate via a CVD technique. Typically, a mixture of GaN, Ga₂O₃, and ZnO and a mixture of ZnO and graphite powder were placed into two separate quartz boats, to be used as precursors. The GaN, Ga₂O₃, and ZnO mixture; the ZnO and graphite mixture; and the Si substrate were placed in a miniature quartz tube closed at one end, which was then inserted into a wide quartz tube in a two-zone furnace. Before high-purity argon (Ar) and ammonia (NH₃) gases flowing from the left to right side of the tube were introduced as a mixture carrier gas, each with a flow rate of 50 sccm, the furnace was evacuated using a high-performance rotary vacuum pump. Then, the temperature of the first zone was first increased to 890°C from room temperature with a ramp rate of 57°C min⁻¹ and maintained at 890°C for 15 min, and afterward heated up to 1,140°C at a heating rate of 16°C min⁻¹. The second zone temperature was first increased to the growth temperature, i.e., 700°C, with a ramp rate of 45°C min⁻¹ when the first zone temperature reached 890°C. The nanowires were synthesized for an optimized growth time of 20 min. To obtain (Ga_{1-x}Zn_x)(N_{1-x}O_x) solid-solution nanowires over the entire composition range, GaN, Ga₂O₃, and ZnO mixtures with different weight ratios of ZnO ranging from 1:1:6 to 1:1:9 were used, while keeping the ZnO and graphite mass ratio (2:1) constant.

Pure ZnO and GaN nanowires were also synthesized on the Au-coated Si (111) substrate using previously reported conditions with slight modifications.^{64,65} Briefly, a 1 g mixture of ZnO and graphite (2:1) as the source material was transferred into a quartz boat placed at the center of the first zone. The precursor vapor was collected on the Si substrate positioned downstream of the precursor boat in the second zone. Before heating up, the furnace was evacuated and then purged with Ar gas. For the growth, Ar and O₂ gases with flow rates of 600 and 10 sccm were used as a mixture carrier gas. The temperatures of the first and second zones were set at 1,050°C and 500°C with ramp rates of 16°C and 30°C min⁻¹, respectively. The optimized growth time for ZnO nanowires was found to be 60 min. GaN nanowires were synthesized using the same furnace. The GaN powder was transferred to a quartz boat and placed in the center of the first zone as the source material. The vapors were collected on the Si substrate in the second zone downstream of the center of the precursor boat. The temperatures of the first and the second zones were set at 1,135°C and 800°C with ramp rates of 16°C and 31°C min⁻¹, respectively. The optimized growth time for GaN nanowires was 60 min.

Cocatalyst loading and optimization

Prior to the photocatalytic overall water-splitting reaction, the as-synthesized solid-solution nanowires were decorated with the Rh/Cr₂O₃ core/shell cocatalysts by photodeposition using a closed photocatalysis reactor under conditions similar to those in the previous reports.⁶⁶ Briefly, the Si (111) substrate with nanowires was placed in a Pyrex chamber containing a solution of 2.5 mL of 0.1 mM Na₃RhCl₆, 12 mL of methanol, and 60 mL of deionized water. The chamber was evacuated and irradiated by visible light ($\lambda \geq 400$ nm) for 15 min, during which Rh(III) was reduced to form Rh nanoparticles and deposited on the (Ga_{1-x}Zn_x)(N_{1-x}O_x) nanowires. For the photodeposition of a Cr₂O₃ shell on the Rh core, the same protocol was followed while using 5 mL of a 0.2 mM K₂CrO₄ solution. To reduce K₂CrO₄ to Cr₂O₃ and photodeposit it on the Rh core, the reactor was exposed to visible light ($\lambda \geq 400$ nm) for 4 h. To optimize the amount of the cocatalyst, different volumes of the Rh and Cr solutions were used for loading Rh/Cr₂O₃ core/shell particles on the nanowires. According to the plot of the loaded amount of the cocatalyst versus the gas evolution rate in Figure S15, 3 mL of the cocatalyst solution was found to be an optimal quantity to obtain the highest catalytic activity.

Physicochemical characterization

SEM images were obtained at the accelerating voltage of 10 kV using a field-emission scanning electron microscope (Hitachi S-4800, Japan). HR-TEM imaging, EDS line-scan profiling, and elemental mapping were done at 200 kV using a transmission electron microscope (Tecnai F20, FEI, USA). XRD patterns were recorded using an X'Pert diffractometer with an operating voltage of 40 kV and an operating current of 40 mA. UV-vis diffused reflectance spectra were taken with the help of a UV-2600 spectrometer equipped with an external diffuse reflectance accessory (DRA-2500) by using a blank Si substrate as a reference. For all the solid-solution nanowires samples, band-gap (E_g) values were obtained from UV-vis absorption spectra by linear extrapolation of the absorption edge to zero absorbance. For the measurement of band energy levels, the samples were analyzed by UPS (Thermo Scientific ESCA Lab 250 Xi). A gas discharge lamp was used for UPS, under helium gas and taking the He I (21.22 eV) emission line. The helium pressure in the analysis chamber during analysis was $\sim 2 \times 10^{-8}$ mbar; data were acquired under the bias of -10 V. The work function and VB edge values were determined from UPS data, while the CB edge values were calculated by subtracting the corresponding VBM from the E_g values.

X-ray absorption data collection, analysis, and modeling

X-ray absorption fine structure (XAFS) analysis of Zn (Ga) K edge was recorded at the XAFS station (Beamline 1W1B) of the Beijing Synchrotron Radiation Laboratory using the grazing-incidence XAFS (GI-XAFS) mode. The beamline provided a focused X-ray beam with energy ranging from 5 to 20 keV, a photon flux on the order of 10^{14} phs s⁻¹ (at 10 keV). The beamline monochromators were calibrated by a Zn metallic foil (K edge at 9,659 eV) before each experiment. GI-XAFS of the samples was collected from -120 to +600 eV relative to the Zn (Ga) K-edge by a 19-element Ge array detector at room temperature. Bragg diffraction peaks from the crystal were avoided by seeking the optimum sample rotation angle and by tuning the grazing-incidence angle. The acquired XAFS data were processed according to the standard procedures using the ATHENA module implemented in the IFEFFIT software packages.⁶⁷

To understand the structure of the ZnO-GaN system, we performed systematic simulations over the Zn and Ga K-edges for short-range ordered and disordered (Ga_{1-x}Zn_x)(N_{1-x}O_x) solid solutions²⁵ by the FEFF9.0 code,⁶⁸ which was based on self-consistent-field potential with muffin-tin approximation. The geometric structures of (Ga_{1-x}Zn_x)(N_{1-x}O_x) supercells with the number ratios of Ga to Zn atoms (N to O atoms)

being 32:4, 25:11, 18:18, 11:25, and 4:32 were optimized within the framework of spin-restricted density functional theory by using the VASP code (Figures S5 and S6).^{69,70} The atomic potential was calculated self-consistently using a spherical cluster of about 120 atoms within a radius of 7.0 Å. And the radius of full multiple scattering computing was 8.0 Å, which was sufficient to achieve a good convergence. For the calculations, the Hedin-Lundqvist exchange-correlation potential was used.

Photocatalytic water-splitting test

Photocatalytic pure-water-splitting reactions were carried out under atmospheric pressure in an airtight Pyrex glass vessel with front irradiation. The cocatalyst-loaded sample with a size of 0.5 cm × 1.0 cm was placed in the vessel to face a xenon lamp (300 W) fitted with a 400 nm cutoff filter. The light intensity (400–780 nm) focused on the sample was ca. 226 mW cm⁻², which was measured with a calibrated fiber-optic spectrometer (Avantes AvaSpec-ULS2048). Prior to the pure-water-splitting reaction, the aqueous solution of H₂SO₄ (200 mL) at pH 4.5⁵⁹ was purged with high-purity nitrogen gas for 30–40 min to remove dissolved oxygen. The water-splitting reaction was started by irradiating the sample with visible light ($\lambda \geq 400$ nm) under stirring using a magnetic stir bar. Sampling the evolved H₂ gas was done using a syringe and analyzed by gas chromatography (7890II, Shanghai Techcomp Ltd, China) with ultra-pure N₂ as the carrier gas. The light-to-hydrogen conversion efficiency (η_{LTH}) was calculated using the following formula:

$$\eta_{LTH} = \frac{R_{H_2} \times \Delta G_{H_2}}{P \times A} \times 100\%,$$

where R_{H_2} , ΔG_{H_2} , P , and A are the rate of hydrogen evolution, the Gibbs energy for the water-splitting reaction, the energy intensity of the incident light, and the irradiated sample area, respectively.

SUPPLEMENTAL INFORMATION

Supplemental information can be found online at <https://doi.org/10.1016/j.matt.2020.12.024>.

ACKNOWLEDGMENTS

The authors acknowledge financial support from the Strategic Priority Research Program of CAS (No. XDB36000000), the Basic Science Center Program for Ordered Energy Conversion of the National Natural Science Foundation of China (No. 51888103), the National Natural Science Foundation of China (Nos. 21872043, 21573049, 21422303), the National Basic Research Plan of China (Nos. 2018YFB1502000, 2016YFA0201600), the Beijing Natural Science Foundation (No. 2142036), the Fundamental Research Funds for the Central Universities (No. NJ2020048), the Startup Fund from Nanjing University of Aeronautics and Astronautics (No. 56SYAH19047), and the Knowledge Innovation Program, Youth Innovation Promotion Association, and Special Program of “One Belt One Road” of CAS.

AUTHOR CONTRIBUTIONS

J.R.G. and K.Z. supervised the project. K.Z. and J.R.G. proposed the research direction. Y.A., K.Z., and S.U.J. designed and performed the experiments. K.Z., J.R.G., Y.A., S.U.J., G.X., M.Z.A., S.U., and Y.X. analyzed and discussed the experimental results. K.Z., T.C., Y.A., S.C., and J.Z. performed the synchrotron experiments and discussed and analyzed the results. K.Z., T.C., and Z.Z. conducted the first principle calculation. K.Z., J.R.G., Y.A., and S.U.J. drafted the manuscript. K.Z., T.C., and Y.A. contributed equally to this work.

DECLARATION OF INTERESTS

The authors declare no competing financial interests.

Received: October 9, 2020

Revised: November 27, 2020

Accepted: December 28, 2020

Published: January 21, 2021

REFERENCES

- Lewis, N.S. (2007). Toward cost-effective solar energy use. *Science* 315, 798–801.
- Turner, J.A. (1999). A realizable renewable energy future. *Science* 285, 687–689.
- Kudo, A., and Miseki, Y. (2009). Heterogeneous photocatalyst materials for water splitting. *Chem. Soc. Rev.* 38, 253–278.
- Chen, X., Shen, S., Guo, L., and Mao, S.S. (2010). Semiconductor-based photocatalytic hydrogen generation. *Chem. Rev.* 110, 6503–6570.
- Maeda, K., and Domen, K. (2007). New non-oxide photocatalysts designed for overall water splitting under visible light. *J. Phys. Chem. C* 111, 7851–7861.
- Chen, S., Takata, T., and Domen, K. (2017). Particulate photocatalysts for overall water splitting. *Nat. Rev. Mater.* 2, 17050.
- Wang, Q., and Domen, K. (2020). Particulate photocatalysts for light-driven water splitting: mechanisms, challenges, and design strategies. *Chem. Rev.* 120, 919–985.
- Pan, C., Takata, T., Nakabayashi, M., Matsumoto, T., Shibata, N., Ikuhara, Y., and Domen, K. (2015). A complex perovskite-type oxynitride: the first photocatalyst for water splitting operable at up to 600 nm. *Angew. Chem. Int. Ed.* 54, 2955–2959.
- Wang, Q., Nakabayashi, M., Hisatomi, T., Sun, S., Akiyama, S., Wang, Z., Pan, Z.H., Xiao, X., Watanabe, T., Yamada, T., et al. (2019). Oxsulfide photocatalyst for visible-light-driven overall water splitting. *Nat. Mater.* 18, 827–832.
- Osterloh, F.E. (2013). Inorganic nanostructures for photoelectrochemical and photocatalytic water splitting. *Chem. Soc. Rev.* 42, 2294–2320.
- Liu, S., Tang, Z.-R., Sun, Y., Colmenares, J.C., and Xu, Y.J. (2015). One-dimension-based spatially ordered architectures for solar energy conversion. *Chem. Soc. Rev.* 44, 5053–5075.
- Yuan, L., Han, C., Yang, M.Q., and Xu, Y.J. (2016). Photocatalytic water splitting for solar hydrogen generation: fundamentals and recent advancements. *Int. Rev. Phys. Chem.* 35, 1–36.
- Ding, Q.Q., Zhang, Y., Chen, X., Fu, X.Q., Chen, D.K., Chen, S.J., Gu, L., Wei, F., Bei, H.B., Gao, Y.F., et al. (2019). Tuning element distribution, structure and properties by composition in high-entropy alloys. *Nature* 574, 223–227.
- Liang, J.S., Ma, F., Hwang, S., Wang, X.X., Sokolowski, J., Li, Q., Wu, G., and Su, D. (2019). Atomic arrangement engineering of metallic nanocrystals for energy-conversion electrocatalysis. *Joule* 3, 956–991.
- Maeda, K., Takata, T., Hara, M., Saito, N., Inoue, Y., Kobayashi, H., and Domen, K. (2005). GaN:ZnO solid solution as a photocatalyst for visible-light-driven overall water splitting. *J. Am. Chem. Soc.* 127, 8286–8287.
- Maeda, K., Teramura, K., Lu, D.L., Takata, T., Saito, N., Inoue, Y., and Domen, K. (2006). Photocatalyst releasing hydrogen from water – Enhancing catalytic performance holds promise for hydrogen production by water splitting in sunlight. *Nature* 440, 295.
- Maeda, K., Teramura, K., Saito, N., Inoue, Y., Kobayashi, H., and Domen, K. (2006). Overall water splitting using (oxy)nitride photocatalysts. *Pure Appl. Chem.* 78, 2267–2276.
- Maeda, K., and Domen, K. (2010). Solid solution of GaN and ZnO as a stable photocatalyst for overall water splitting under visible light. *Chem. Mater.* 22, 612–623.
- Ohno, T., Bai, L., Hisatomi, T., Maeda, K., and Domen, K. (2012). Photocatalytic water splitting using modified GaN:ZnO solid solution under visible light: long-time operation and regeneration of activity. *J. Am. Chem. Soc.* 134, 8254–8259.
- Maeda, K., Teramura, K., and Domen, K. (2008). Effect of post-calcination on photocatalytic activity of $(\text{Ga}_{1-x}\text{Zn}_x)(\text{N}_{1-x}\text{O}_x)$ solid solution for overall water splitting under visible light. *J. Catal.* 254, 198–204.
- Huda, M.N., Yan, Y., Wei, S.-H., and Al-Jassim, M.M. (2008). Electronic structure of ZnO:GaN compounds: Asymmetric bandgap engineering. *Phys. Rev. B* 78, 195204.
- Chen, H., Wang, L., Bai, J., Hanson, J.C., Warren, J.B., Muckerman, J.T., Fujita, E., and Rodriguez, J.A. (2010). In situ XRD studies of ZnO/GaN mixtures at high pressure and high temperature: synthesis of Zn-rich $(\text{Ga}_{1-x}\text{Zn}_x)(\text{N}_{1-x}\text{O}_x)$ photocatalysts. *J. Phys. Chem. C* 114, 1809–1814.
- Jensen, L.L., Muckerman, J.T., and Newton, M.D. (2008). First-principles studies of the structural and electronic properties of the $(\text{Ga}_{1-x}\text{Zn}_x)(\text{N}_{1-x}\text{O}_x)$ solid solution photocatalyst. *J. Phys. Chem. C* 112, 3439–3446.
- Lee, K., Tienes, B.M., Wilker, M.B., Schnitzenbaumer, K.J., and Dukovic, G. (2012). $(\text{Ga}_{1-x}\text{Zn}_x)(\text{N}_{1-x}\text{O}_x)$ nanocrystals: visible absorbers with tunable composition and absorption spectra. *Nano Lett.* 12, 3268–3272.
- Li, L., Muckerman, J.T., Hybertsen, M.S., and Allen, P.B. (2011). Phase diagram, structure, and electronic properties of $(\text{Ga}_{1-x}\text{Zn}_x)(\text{N}_{1-x}\text{O}_x)$ solid solutions from DFT-based simulations. *Phys. Rev. B* 83, 134202.
- Li, Y., Zhu, L., Yang, Y., Song, H., Lou, Z., Guo, Y., and Ye, Z. (2015). A full compositional range for a $(\text{Ga}_{1-x}\text{Zn}_x)(\text{N}_{1-x}\text{O}_x)$ nanostructure: high efficiency for overall water splitting and optical properties. *Small* 11, 871–876.
- Wang, J.P., Huang, B.B., Wang, Z.Y., Wang, P., Cheng, H.F., Zheng, Z.K., Qin, X.Y., Zhang, X.Y., Dai, Y., and Whangbo, M.H. (2011). Facile synthesis of Zn-rich $(\text{GaN})_{1-x}(\text{ZnO})_x$ solid solutions using layered double hydroxides as precursors. *J. Mater. Chem.* 21, 4562–4567.
- Liu, J., Fernandez-Serra, M.V., and Allen, P.B. (2016). Special quasiordered structures: role of short-range order in the semiconductor alloy $(\text{GaN})_{1-x}(\text{ZnO})_x$. *Phys. Rev. B* 93, 054207.
- Maeda, K., Teramura, K., Takata, T., Hara, M., Saito, N., Toda, K., Inoue, Y., Kobayashi, H., and Domen, K. (2005). Overall water splitting on $(\text{Ga}_{1-x}\text{Zn}_x)(\text{N}_{1-x}\text{O}_x)$ solid solution photocatalyst: relationship between physical properties and photocatalytic activity. *J. Phys. Chem. B* 109, 20504–20510.
- Wei, W., Dai, Y., Yang, K.S., Guo, M., and Huang, B.B. (2008). Origin of the visible light absorption of GaN-Rich $\text{Ga}_{1-x}\text{Zn}_x\text{N}_{1-x}\text{O}_x$ ($x=0.125$) solid solution. *J. Phys. Chem. C* 112, 15915–15919.
- Hirai, T., Maeda, K., Yoshida, M., Kubota, J., Ikeda, S., Matsumura, M., and Domen, K. (2007). Origin of visible light absorption in GaN-Rich $(\text{Ga}_{1-x}\text{Zn}_x)(\text{N}_{1-x}\text{O}_x)$ photocatalysts. *J. Phys. Chem. C* 111, 18853–18855.
- Wang, S.Z., and Wang, L.W. (2010). Atomic and electronic structures of GaN/ZnO Alloys. *Phys. Rev. Lett.* 104, 065501.
- Sun, X., Maeda, K., Le Faucheur, M., Teramura, K., and Domen, K. (2007). Preparation of $(\text{Ga}_{1-x}\text{Zn}_x)(\text{N}_{1-x}\text{O}_x)$ solid-solution from ZnGa_2O_4 and ZnO as a photo-catalyst for overall water splitting under visible light. *Appl. Catal. A-gen.* 327, 114–121.
- Chen, H., Wen, W., Wang, Q., Hanson, J.C., Muckerman, J.T., Fujita, E., Frenkel, A.I., and Rodriguez, J.A. (2009). Preparation of $(\text{Ga}_{1-x}\text{Zn}_x)(\text{N}_{1-x}\text{O}_x)$ photocatalysts from the reaction of NH_3 with $\text{Ga}_2\text{O}_3/\text{ZnO}$ and ZnGa_2O_4 : in situ time-resolved XRD and XAFS studies. *J. Phys. Chem. C* 113, 3650–3659.
- Dasgupta, N.P., Sun, J.W., Liu, C., Brittman, S., Andrews, S.C., Lim, J., Gao, H.W., Yan, R.X., and Yang, P.D. (2014). 25th anniversary article:

- semiconductor nanowires-synthesis, characterization, and applications. *Adv. Mater.* 26, 2137–2184.
36. Han, W.Q., Zhang, Y., Nam, C.Y., Black, C.T., and Mendez, E.E. (2010). Growth and electronic properties of GaN/ZnO solid solution nanowires. *Appl. Phys. Lett.* 97, 083108.
 37. Liu, B., Bando, Y., Liu, L., Zhao, J., Masanori, M., Jiang, X., and Golberg, D. (2013). Solid-solution semiconductor nanowires in pseudobinary systems. *Nano Lett.* 13, 85–90.
 38. Hahn, C., Fardy, M.A., Nguyen, C., Natera-Comte, M., Andrews, S.C., and Yang, P.D. (2012). Synthesis and photocatalytic properties of single crystalline $(\text{Ga}_{1-x}\text{Zn}_x)(\text{N}_{1-x}\text{O}_x)$ nanotubes. *Isr. J. Chem.* 52, 1111–1117.
 39. Li, J., Yang, W.J., Wu, A.M., Zhang, X.L., Xu, T.T., and Liu, B.D. (2020). Band-gap tunable 2D hexagonal $(\text{GaN})_{1-x}(\text{ZnO})_x$ solid-solution nanosheets for photocatalytic water splitting. *ACS Appl. Mater. Inter.* 12, 8583–8591.
 40. Yao, B.D., Chan, Y.F., and Wang, N. (2002). Formation of ZnO nanostructures by a simple way of thermal evaporation. *Appl. Phys. Lett.* 81, 757–759.
 41. Li, J., Liu, B.D., Wu, A.M., Yang, B., Yang, W.J., Liu, F., Zhang, X.L., An, V., and Jiang, X. (2018). Composition and band gap tailoring of crystalline $(\text{GaN})_{1-x}(\text{ZnO})_x$ solid solution nanowires for enhanced photoelectrochemical performance. *Inorg. Chem.* 57, 5240–5248.
 42. Tongying, P., Lu, Y.-G., Hall, L.M.G., Lee, K., Sulima, M., Ciston, J., and Dukovic, G. (2017). Control of elemental distribution in the nanoscale solid-state reaction that produces $(\text{Ga}_{1-x}\text{Zn}_x)(\text{N}_{1-x}\text{O}_x)$ nanocrystals. *ACS Nano* 11, 8401–8412.
 43. Wu, A., Li, J., Liu, B., Yang, W., Jiang, Y., Liu, L., Zhang, X., Xiong, C., and Jiang, X. (2017). Band-gap tailoring and visible-light-driven photocatalytic performance of porous $(\text{GaN})_{1-x}(\text{ZnO})_x$ solid solution. *Dalton. Trans.* 46, 2643–2652.
 44. Adeli, B., and Taghipour, F. (2013). A review of synthesis techniques for gallium-zinc oxynitride solar-activated photocatalyst for water splitting. *ECS J. Solid State SC* 2, Q118–Q126.
 45. Katagiri, K., Hayashi, Y., Yoshiyuki, R., Inumaru, K., Uchiyama, T., Nagata, N., Uchimoto, Y., Miyoshi, A., and Maeda, K. (2018). Mechanistic Insight on the formation of GaN:ZnO solid solution from Zn-Ga layered double hydroxide using Urea as the nitriding Agent. *Inorg. Chem.* 57, 13953–13962.
 46. Denton, A.R., and Ashcroft, N.W. (1991). Vegard's law. *Phys. Rev. A* 43, 3161–3164.
 47. Wu, Y., and Yang, P. (2001). Direct observation of vapor-liquid-solid nanowire growth. *J. Am. Chem. Soc.* 123, 3165–3166.
 48. Park, K., Lee, J.A., Im, H.S., Jung, C.S., Kim, H.S., Park, J., and Lee, C.L. (2014). GaP-ZnS pseudobinary alloy nanowires. *Nano Lett.* 14, 5912–5919.
 49. Yang, W.J., Liu, B.D., Yang, B., Wang, J.Y., Sekiguchi, T., Thorsten, S., and Jiang, X. (2015). Pseudobinary solid-solution: an alternative way for the bandgap engineering of semiconductor nanowires in the case of GaP-ZnSe. *Adv. Funct. Mater.* 25, 2543–2551.
 50. Ciatto, G., D'Acapito, F., Grenouillet, L., Mariette, H., De Salvador, D., Bisognin, G., Carboni, R., Floreano, L., Gotter, R., Mobilio, S., and Boscherini, F. (2003). Quantitative determination of short-range ordering in $\text{In}_x\text{Ga}_{1-x}\text{As}_{1-y}\text{N}_y$. *Phys. Rev. B* 68, 161201.
 51. Lordi, V., Gambin, V., Friedrich, S., Funk, T., Takizawa, T., Uno, K., and Harris, J.S. (2003). Nearest-neighbor configuration in $(\text{GaN})(\text{NAs})$ probed by X-ray absorption spectroscopy. *Phys. Rev. Lett.* 90, 145505.
 52. Chen, D.P., Neufeind, J.C., Koczkur, K.M., Bish, D.L., and Skrabalak, S.E. (2017). Role of short-range chemical ordering in $(\text{GaN})_{1-x}(\text{ZnO})_x$ for photodriven oxygen evolution. *Chem. Mater.* 29, 6525–6535.
 53. Guglieri, C., and Chaboy, J. (2010). Characterization of the ZnO-ZnS interface in THIOL-capped ZnO nanoparticles exhibiting anomalous magnetic properties. *J. Phys. Chem. C* 114, 19629–19634.
 54. Guglieri, C., Laguna-Marcos, M.A., García, M.A., Carmona, N., Céspedes, E., García-Hernández, M., Espinosa, A., and Chaboy, J. (2012). XMCD proof of ferromagnetic behavior in ZnO nanoparticles. *J. Phys. Chem. C* 116, 6608–6614.
 55. Jain, A., Ong, S.P., Hautier, G., Chen, W., Richards, W.D., Dacek, S., Cholia, S., Gunter, D., Skinner, D., Ceder, G., and Persson, K.A. (2013). Commentary: the Materials Project: a materials genome approach to accelerating materials innovation. *APL Mater.* 1, 011002.
 56. Xu, Y., and Schoonen, M.A.A. (2000). The absolute energy positions of conduction and valence bands of selected semiconducting minerals. *Am. Mineral.* 85, 543–556.
 57. Mäder, K.A., and Zunger, A. (1995). Short- and long-range-order effects on the electronic properties of III-V semiconductor alloys. *Phys. Rev. B* 51, 10462–10476.
 58. Maeda, K., Teramura, K., Masuda, H., Takata, T., Saito, N., Inoue, Y., and Domen, K. (2006). Efficient overall water splitting under visible-light irradiation on $(\text{Ga}_{1-x}\text{Zn}_x)(\text{N}_{1-x}\text{O}_x)$ dispersed with Rh-Cr mixed-oxide nanoparticles: effect of reaction conditions on photocatalytic activity. *J. Phys. Chem. B* 110, 13107–13112.
 59. Maeda, K., Masuda, H., and Domen, K. (2009). Effect of electrolyte addition on activity of $(\text{Ga}_{1-x}\text{Zn}_x)(\text{N}_{1-x}\text{O}_x)$ photocatalyst for overall water splitting under visible light. *Catal. Today* 147, 173–178.
 60. Maeda, K., Teramura, K., Lu, D.L., Saito, N., Inoue, Y., and Domen, K. (2006). Noble-metal/Cr₂O₃ core/shell nanoparticles as a cocatalyst for photocatalytic overall water splitting. *Angew. Chem. Int. Ed.* 45, 7806–7809.
 61. Maeda, K., Teramura, K., Lu, D.L., Saito, N., Inoue, Y., and Domen, K. (2007). Roles of Rh/Cr₂O₃ (core/shell) nanoparticles photodeposited on visible-light-responsive $(\text{Ga}_{1-x}\text{Zn}_x)(\text{N}_{1-x}\text{O}_x)$ solid solutions in photocatalytic overall water splitting. *J. Phys. Chem. C* 111, 7554–7560.
 62. Hisatomi, T., Maeda, K., Takanabe, K., Kubota, J., and Domen, K. (2009). Aspects of the water splitting mechanism on $(\text{Ga}_{1-x}\text{Zn}_x)(\text{N}_{1-x}\text{O}_x)$ photocatalyst modified with Rh_{2-y}Cr_yO₃ cocatalyst. *J. Phys. Chem. C* 113, 21458–21466.
 63. Wang, Q., Hisatomi, T., Jia, Q.X., Tokudome, H., Zhong, M., Wang, C.Z., Pan, Z.H., Takata, T., Nakabayashi, M., Shibata, N., et al. (2016). Scalable water splitting on particulate photocatalyst sheets with a solar-to-hydrogen energy conversion efficiency exceeding 1%. *Nat. Mater.* 15, 611–615.
 64. Xu, C.H., Leung, K., Hu, J., and Surya, C. (2012). Synthetics of ZnO nanowires on GaN micro-pyramids by gold catalyst. *Mater. Lett.* 74, 100–103.
 65. Yang, Y., Ling, Y., Wang, G., Lu, X., Tong, Y., and Li, Y. (2013). Growth of gallium nitride and indium nitride nanowires on conductive and flexible carbon cloth substrates. *Nanoscale* 5, 1820–1824.
 66. Kibria, M.G., Nguyen, H.P.T., Cui, K., Zhao, S., Liu, D., Guo, H., Trudeau, M.L., Paradis, S., Hakima, A.-R., and Mi, Z. (2013). One-step overall water splitting under visible light using multiband InGaN/GaN nanowire heterostructures. *ACS Nano* 7, 7886–7893.
 67. Ravel, B., and Newville, M. (2005). ATHENA, ARTEMIS, HEPHAESTUS: data analysis for X-ray absorption spectroscopy using IFEFFIT. *J. Synchrotron Radiat.* 12, 537–541.
 68. Jorissen, K., and Rehr, J.J. (2013). New developments in FEFF: FEFF9 and JEFF. *J. Phys. Conf. Ser.* 430, 012001.
 69. Kresse, G., and Furthmüller, J. (1996). Efficient iterative schemes for ab initio total-energy calculations using a plane-wave basis set. *Phys. Rev. B* 54, 11169–11186.
 70. Kresse, G., and Furthmüller, J. (1996). Efficiency of ab-initio total energy calculations for metals and semiconductors using a plane-wave basis set. *Comp. Mater. Sci.* 6, 15–50.